PCCP

ROYAL SOCIETY OF CHEMISTRY

PAPER

View Article Online
View Journal | View Issue

Cite this: *Phys. Chem. Chem. Phys.*, 2024, **26**, 7416

The role of the oxime group in the excited state deactivation processes of indirubin†

Danîela C. Nobre,[a] Estefanía Delgado-Pinar,[ab] Carla Cunha[a] and J. Sérgio Seixas de Melo *[a]

Received 30th October 2023,
Accepted 6th February 2024

DOI: 10.1039/d3cp05260e

rsc.li/pccp

The introduction of an oxime group into indirubin (INR) derivatives, including INROx, MINROx, and 6-BrINROx, and its impact on the spectral and photophysical properties of INR was investigated using a combination of fast-transient absorption (fs-TA/fs-UC) and steady-state fluorescence techniques. The oxime group introduces structural modifications that promote a rapid keto–enol tautomeric equilibrium and enhance the excited-state proton transfer (ESPT) process compared to its analogue, INR. In the oxime–indirubin derivatives investigated, the ESPT process is notably more efficient than what is observed in INR and indigo, occurring extremely fast (<1 ps) in all solvents, except for the viscous solvent glycerol. The more rapid deactivation mechanism precludes the formation of an intermediate species (*syn*-rotamer), as observed with INR. These findings are corroborated by time-dependent density functional theory (TDDFT) calculations. The work demonstrates that introducing an oxime group to INR, whether in nature or in the laboratory, results in an enhancement of its photostability.

Introduction

While typically associated with plant products, indigo (IND) and the indirubins (INRs) have been documented in four distinct sources: (i) various plants, including *Baphicacanthus cusia*, *Polygonum tinctorium*, *Isatis indigotica*, *Indigofera suffruticosa*, and *Indigofera tinctoria*; (ii) several marine mollusks, primarily within the *Muricidae* family of gastropods; (iii) natural or recombinant bacteria; and (iv) human urine.[1–5]

Indirubin, a dark-red 3,2′-bisindole isomer of indigo, is also recognized as an active ingredient in Danggui Longhui Wan, a Traditional Chinese Medicine (TCM) employed in the treatment of chronic diseases like chronic myelogenous leukemia.[6–10] In addition to cyclin-dependent kinases (CDKs), indirubins have been observed to interact with glycogen synthase kinase-3 (GSK-3), aurora kinases, and the aryl hydrocarbon receptor (AhR), also known as the dioxin receptor.[2,3,11–13] Over the past decade, several indirubin analogs have been synthesized to enhance this promising drug scaffold.[14,15] Incorporation of oxime groups enhances the kinase inhibitory activity of natural compounds.[16,17] These findings have prompted a range of studies related to their physiological and pharmacological functions. Several indirubin derivatives have been synthesized and characterized for their kinase inhibition and anticancer properties.[18]

In this context, incorporating an oxime group into the backbone has proven to be a viable strategy for developing cytotoxic agents, and numerous oxime derivatives have been recognised for their therapeutic activity against cancer and neurodegenerative disorders.[16]

In the last two decades, a significant number of oximes have been documented to possess valuable pharmaceutical properties, including compounds with antibacterial, anticancer, anti-arthritis, anti-inflammatory activities, and anti-human immunodeficiency (HIV) agents capable of inhibiting HIV protease.[16,19] The oxime group contains two H-bond acceptors (nitrogen and oxygen atoms) and one H-bond donor (OH group), in contrast to carbonyl groups, which have only one H-bond acceptor. This distinctive characteristic, combined with the high polarity of oxime groups, can lead to a notably different interaction mode with receptor binding sites when compared to corresponding carbonyl compounds, even in cases of slight differences in the overall size and shape of the compound.[16]

Considerable research has been undertaken on indirubins and oxime–indirubin derivatives, with a primary focus on biological aspects of these compounds. Nonetheless, their photophysical and photochemical properties have mostly remained unexplored.

This work involves the synthesis and comprehensive examination of various oxime–indirubin derivatives, which have shown promise for various biological applications. The study is focused on exploring the impact of substituting the oxime group on the electronic spectral, photophysical, and photochemical properties of the compounds in comparison to indirubin.

[a] *University of Coimbra, CQC-ISM, Department of Chemistry, P3004-535 Coimbra, Portugal. E-mail: sseixas@ci.uc.pt*
[b] *Instituto de Ciencia Molecular, Departamento de Química Inorgánica, Universidad de Valencia, C/Catedrático José Beltrán 2, 46980, Paterna, Valencia, Spain*

† Electronic supplementary information (ESI) available. See DOI: https://doi.org/10.1039/d3cp05260e

The observed properties and behavior were further elucidated through TDDFT computational studies.

Results and discussion

Synthesis of the oxime–indirubin derivatives: general synthetic procedure

The synthesis of the indirubin-3′-oxime derivatives was carried out following a modified procedure described elsewhere.[20] The corresponding indirubin derivative (100 mg) was placed in a round-bottom flask, and 10 mL of pyridine was added. After 5 minutes of stirring, hydroxylamine hydrochloride (10 equiv.) was introduced, and the solution was heated under reflux for 2 h. Then, the solvent was evaporated under reduced pressure, and the residue was washed with the appropriate solvent, see Scheme 1. The molecular structures of all the indirubin derivatives and oxime–indirubin derivatives were confirmed by ^{1}H and ^{13}C nuclear magnetic resonance (NMR) spectroscopy and further by high resolution mass spectrometry (HRMS), please see Fig. SI1–SI16 (ESI†). The obtained data were found in accordance with the structure proposed.

The influence of the oxime group on the spectral and photophysical properties of indirubin (INR)

Absorption and fluorescence spectra of oxime–indirubin derivatives (INROx, 6-BrINROx, and MINROx) were recorded in various organic solvents with different dielectric constant (ε) and viscosities (η) at room temperature (T = 293 K).

Fig. 1 presents the absorption and fluorescence emission spectra of the oxime–indirubin derivatives in dioxane. For the sake of comparison, previously acquired data for indirubin (INR) in dioxane were also considered.[21]

Table 1 highlights important characteristics of the oxime–indirubin derivatives, including that (i) the absorption wavelength maxima of oxime–indirubin derivatives are blue-shifted by approximately 24–40 nm, when compared to indirubin (INR). This indicates that (i) the fundamental core responsible for the highest occupied molecular orbital (HOMO) – lowest unoccupied molecular orbital (LUMO) transition is affected by the oxime group substitution; (ii) in comparison with INR, it is noteworthy that oxime–indirubin derivatives exhibit a significantly larger Stokes shift value. Indeed, oxime–indirubin derivatives display a broad fluorescence spectrum, providing direct evidence that the emission spectra likely involve convolution of more than one contributing species, with a faster keto–enol equilibrium compared to indirubin; (iii) also, in the oxime–indirubin derivatives, the substituent (bromide-, methyl- or non-substituted) and the polarity of the solvents do not appear to interfere significantly with the absorption and emission maxima.

The introduction of the oxime group in oxime–indirubin derivatives results in significant electronic spectral and photophysical changes when compared to INR. These changes arise from distinct contributions to the potential energy curves of the ground and excited states of the compounds. These shows that the deactivation mechanism varies between INR and INROx. Additional insights will be obtained from the time-resolved data presented in Table 2 and will be explained at the light of the DFT and TDDFT calculations.

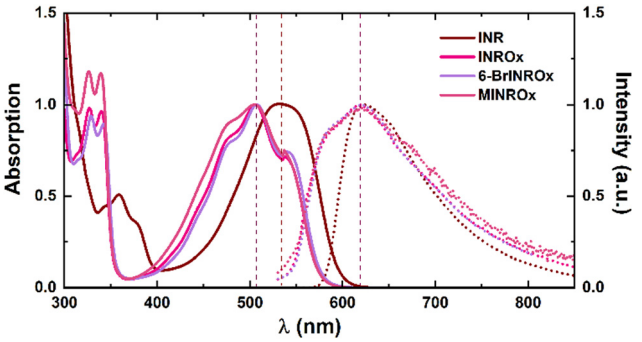

Fig. 1 Normalized absorption (solid line) and fluorescence emission (dashed line) spectra of INROx, 6-BrINROx and MINROx in dioxane at room temperature. Indirubin (INR) spectra are also presented for comparison. The dashed vertical lines are just meant to be guidelines for the eye.

Table 1 Spectroscopic properties, including absorption wavelength maxima (λ_{max}^{abs}), fluorescence emission (λ_{max}^{em}) and Stokes shift (Δ_{SS}) for INROx, 6-BrINROx and MINROx in different organic solvents at T = 293 K. For indirubin (INR) the same parameters are also presented for comparison. The solvent properties (viscosity, η, in cP and dielectric constant, ε) are also given

Compound	η	ε	Solvent	λ_{max}^{abs} (nm)	λ_{max}^{em} (nm)	Δ_{SS} (cm^{-1})
INR[a]	1.20	2.209	Dx	530	640	3243
	0.58	7.58	2-MeTHF	531	635	3084
	0.92	36.7	DMF	546	638	2641
	1.41	42.5	Glycerol	548	676	3455
INROx	1.20	2.209	Dx	506	617	3555
	0.48	7.58	THF	507	616	3490
	0.92	36.7	DMF	506	616	3529
	0.33	37.5	ACN	502	620	3791
	1.41	42.5	Glycerol	510	620	3479
6-BrINROx	1.20	2.209	Dx	507	617	3516
	0.48	7.58	THF	507	618	3543
	0.92	36.7	DMF	506	622	3686
	0.33	37.5	ACN	503	620	3752
MINROx	1.20	2.209	Dx	507	620	3595
	0.48	7.58	THF	507	616	3490
	0.92	36.7	DMF	507	624	3698
	0.33	37.5	ACN	502	620	3791

[a] Data from ref. 21.

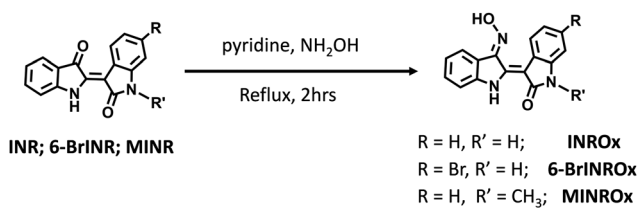

Scheme 1 Synthetic pathway for the synthesis of the oximes: indirubin–3′-oxime (INROx), 6-bromoindirubin-3′-oxime (6-BrINROx) and *N*-methylindirubin-3′-oxime (MINROx).

Table 2 Photophysical data including fluorescence quantum yields (ϕ_F), fluorescence lifetimes (τ_F), rate constants (k_F, k_{NR}) for the oxime–indirubin derivatives (INROx, 6-BrINROx and MINROx) in different organic solvents at T = 293 K. For indirubin (INR) data in dioxane (Dx) and glycerol is shown for comparison

Compound	Solvent	ϕ_F	τ_F (ps)	k_F (s^{-1}) × 10^7	k_{NR} (s^{-1}) × 10^{11}	k_{NR}/k_F × 10^4
INR	Dx	0.0020	38	5.26	0.263	499
	Glycerol	0.0043	50	8.60	0.199	232
INROx	Dx	0.00004	6.8	0.587	1.47	0.0025
	THF	0.00001	4.9	0.200	2.00	0.010
	ACN	0.00001	3.0	0.330	3.30	0.010
	Glycerol	0.00800	93	8.60	0.11	124
6-BrINROx	Dx	0.00005	7.9	0.637	1.27	0.002
	THF	0.00002	5.6	0.357	1.79	0.005
	ACN	0.00001	4.1	0.242	2.42	0.010
MINROx	Dx	0.00001	6.8	0.147	1.47	0.010
	THF	0.00001	4.6	0.217	2.17	0.010
	ACN	0.00005	3.5	1.4	2.86	0.002

Photophysical data, including fluorescence quantum yields (ϕ_F), fluorescence lifetimes (τ_F) and radiative (k_F) and radiationless rate constants (k_{NR}) for the oxime–indirubin derivatives are provided in Table 2. When comparing the oxime–indirubin derivatives to the parent compound (INR), three main observations can be highlighted: (i) oxime–indirubin derivatives exhibit fluorescence quantum yields that are at least one order of magnitude lower than INR; (ii) quantum yield values increase significantly with the increase of the viscosity of the solvent; (iii) in dioxane, the lifetimes are shorter for the oxime–indirubin derivatives, consistent with an ultrafast keto–enol tautomerization equilibrium.

Very often, molecules capable of undergoing excited-state proton transfer (ESPT) have the possibility to establish intramolecular hydrogen bonding interactions between a hydrogen-bond donor (*e.g.*, –OH and NH_2) and a hydrogen-bond acceptor (*e.g.*, C=N– and C=O).[22–32] Tautomerism is a form of isomerization involving species that can easily interconvert. One of the most common type of tautomerism is prototropic tautomerism, which involves a shift in the position of a proton within a molecule.[28,33–36] Even though it may seem like a subtle change, this process leads to substantial modifications in chemical bonding and polarity, ultimately determining molecular properties.

To confirm the presence of an efficient ESPT mechanism in the oxime–indirubin derivatives, femtosecond transient absorption (fs-TA) and femtosecond Up-Conversion (fs-UC) spectroscopy experiments were carried out in various solvents. The fs-TA experiments were carried out in the 440–800 nm range, covering various aerated solvents with different viscosities and dielectric constants. An excitation wavelength of 500 nm was employed for the oxime–indirubin derivatives,

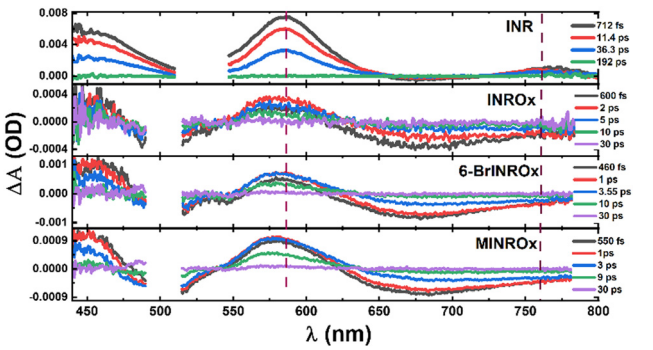

Fig. 2 Time-resolved transient absorption data for indirubin and oxime–indirubin derivatives in dioxane obtained with λ_{exc} = 500 nm and 530 nm at T = 293 K. The vertical dashed line is just meant to be a guideline to the eye, showing the spectral shift of the ESA band for each compound.

Table 3 Decay time values, τ_i, obtained from femtosecond Transient Absorption (fs-TA) and femtosecond fluorescence Up-Conversion (fs-UC) measurements for INR, INROx, 6-BrINROx, and MINROx at T = 293 K in solvents with varying polarity and viscosity. The values presented result from Global Analysis of the data. Table with associated errors is given in ESI (Table SI1)

		fs-TA		fs-UC	
Comp.	Solvent	τ_1 (ps)	τ_2 (ps)	τ_1 (ps)	τ_2 (ps)
INR[a]	Dx	—	38	3	37
	MeOH	2	12	—	—
	DMF	1.8	14	1	8
	Glycerol	16	50	—	—
INROx	Dx	0.80[b]	6.81	0.59	4.03
	THF	0.74[b]	4.99	0.48	3.47
	MeOH	0.72[b]	3.71	—	—
	DMF	0.61[b]	3.28	—	—
	ACN	0.63[b]	3.03	0.58	2.26
	Glycerol	4.03	92.9	—	—
6-BrINROx	Dx	1.12[b]	7.85	0.9	4.69
	THF	0.93[b]	5.60	0.7	3.29
	DMF	0.91[b]	5.28	—	—
	ACN	0.42[b]	4.13	0.6	2.53
MINROx	Dx	0.80[b]	6.79	0.34	4.07
	THF	0.58[b]	4.61	0.5	4
	DMF	0.59[b]	4.39	—	—
	ACN	0.50[b]	3.50	0.3	2.23

[a] Data from ref. 21. [b] The decay component is associated to a negative amplitude (rise-time).

whereas for INR, excitation was performed at 530 nm.[21] Fig. 2 displays the fs-TA spectrum for INROx, MINROx and 6-BrINROx in dioxane. The transient spectrum for INR in dioxane has been previously described.[21]

For the oxime–indirubin derivatives, the fs-TA spectra exhibit positive and broad transient absorption bands in the 530–630 nm range, with maxima at around 580 nm, attributed to an excited singlet-state absorption (ESA). This is accompanied by a negative band in the long wavelength region (640–730 nm) of the spectra, associated to stimulated emission (SE). A bleaching of the ground-state absorption (GSA) in the 440–480 nm range is observed. Comparable variations in the transient absorption bands were noted for the oxime–indirubin derivatives in the other studied solvents.

Characteristic fs-TA data is provided in Table 3. The global analysis of the time-resolved data yields the best-fit results with a bi-exponential decay law, indicating the presence of two excited species for all compounds. In the case of INR, in dioxane, two ESA bands are observed at ~580–600 nm and 775 nm, which disappear after 38 ps. For the oxime–indirubin derivatives, the fs-TA spectra in dioxane shows one ESA band, observed at ~545–630 nm, which now disappear after ~7–8 ps. Both the τ_1 (associated with the formation of the keto species and decaying in approximately 1 ps, *i.e.*, – an ultrafast proton transfer) and τ_2 (associated with the enol species decaying within 3–8 ps) decay time values, obtained in various organic solvents for the oxime–indirubin derivatives are remarkably fast, especially when compared to the values observed with INR (see Table 3). These results further validate that the significant blue-shift of the fluorescence, observed with the oxime–indirubin derivatives when compared to indirubin, is attributed to an efficient excited-state proton transfer (ESPT) process with high proton transfer rate constant values. In glycerol, formation of the enol species is hindered by the solvent's viscosity, leading to a more efficient radiative decay channel, as indicated by the increase in the ϕ_F value (and in the radiative rate constant).

In the oxime–indirubin derivatives, the absorption occurs from the stable keto (K) form in the S_0 state, while the emission arises from the favored enol (E*) isomer in the S_1 state, indicating significant structural changes in the excited state (ES) and, consequently, an increase in the Stokes shift value. ESPT can be considered as a very fast phototautomerization process occurring along with a strong intramolecular hydrogen bond between two atoms presenting acidities/basicities that are significantly influenced upon electronic excitation. This implies the presence of an even more efficient ESPT process in the oxime–indirubin derivatives compared to indirubin, possibly due to a relatively lower potential energy barrier. Fig. SI17 (ESI†) depicts the energy difference between the ground state and the first keto singlet excited state (K-S_1 → K-S_0) for INR and INROx in dioxane.

Table 3 shows that the two decay components (τ_1 and τ_2), corresponding to the presence of the keto and enol forms of the studied compounds, are consistently obtained in different time-resolved experiments (fs-TA and fs-UC). The nature of the species associated with these two decay times will be further elucidated in the context of DFT calculations (as will be discussed below).

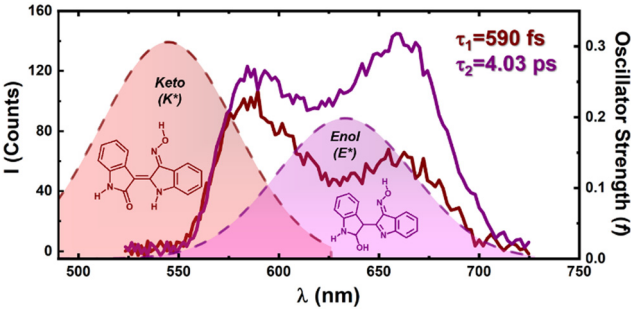

Fig. 3 fs time-resolved Up-Conversion, fs-UC, (solid line) data for INROx in dioxane obtained with λ_{exc} = 500 nm at T = 293 K. The dashed lines and bands in wine and purple show the bands based on the emission maximum calculated (from TDDFT) for the keto (wine line) and enol (purple line) species. See text for more details.

As seen in Fig. 3, the fs Up-Conversion spectra in dioxane for the oxime–indirubin derivative INROx display two bands, K* and E*. For $\tau < 1$ ps, the K* and E* coexist, with the former being more intense. For $\tau > 1$ ps, E* becomes dominant.

The presence of these two species is consistent with the band maxima predicted by TDDFT, confirming that the enol form is the prevailing tautomer in solution for time values > 1 ps (as indicated in Table 3) and is dominant under steady-state conditions (Fig. 1).

TDDFT calculations

A more comprehensive set of density functional (DFT) data was acquired to obtain a deeper insight into the type of structures existent in the ground and excited state and to offer a rational explanation for the experimentally obtained data (both steady-state and time-resolved). INROx was employed to explore various conformational structures (see Fig. SI18, ESI†). The optimized geometries of the oxime–indirubin conformers can be readily obtained, and their energies calculated (see Fig. SI19 for structures, ESI†). Among the investigated structures, and after obtaining the most stable structure and conformer, the various molecular geometries were optimized using DFT calculations, and the primary transitions for both absorption and emission were analyzed.

Fig. SI19 (ESI†) illustrates the most energetically stable conformer for the investigated oxime–indirubin derivatives in dioxane. Fig. SI20 (ESI†) maps the orbital contours of the highest occupied molecular orbital (HOMO) and lowest unoccupied molecular orbital (LUMO) for INR and INROx in dioxane. In INROx the HOMO to LUMO transition retains the nature of the donor and acceptor groups observed in INR; however, the comparison between the HOMO and LUMO of the two compounds shows that the HOMO is found, with INROx, to be energetically lower. However, the most interesting feature in INROx is found in the hydrogen bond N–H···O=C distance, with a value of 174 pm in S_0 (compared to 185 pm for INR), whereas in S_1, the distance is 162 pm (close to that found

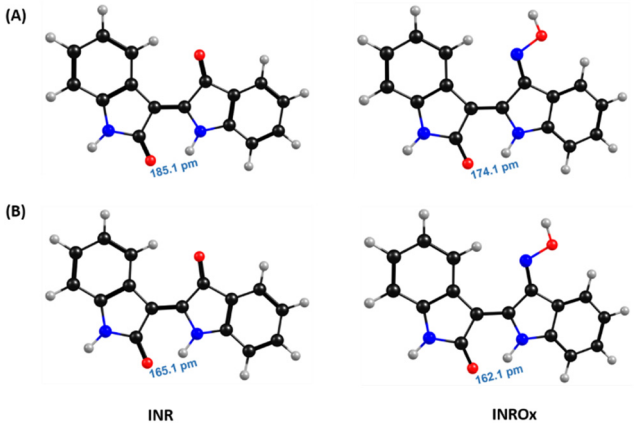

Fig. 4 Optimized structures in the S_0 (A) and S_1 (B) electronic states of INR and INROx, in dioxane. The bond distance between the oxygen in C=O and the hydrogen in N–H decreases from 185.1 pm in S_0 to 165.1 pm in S_1 and 174.1 pm in S_0 to 162.1 pm in S_1, for INR and INROx, respectively; see text for more details.

for INR of 165 pm), as shown in Fig. 4. This shows that for INROx, when compared to INR, this distance is shorter in S_0 and approximately identical in S_1. Moreoever, and in general, the bonding distance between the oxygen in C=O and the hydrogen in N–H decreases with increasing polarity (see Table SI2 in ESI† for all oxime–indirubin derivatives, in different solvents). Indeed, and as observed with INR, the proximity of the amine hydrogen, in the half-indigo moiety, and the keto oxygen, in the isatin moiety, significantly affects the photophysical properties of this molecule. Indeed, in the excited state, the formed N–H···O hydrogen bond allows the proton, from the isatin moiety, to be transferred to the carbonyl group.

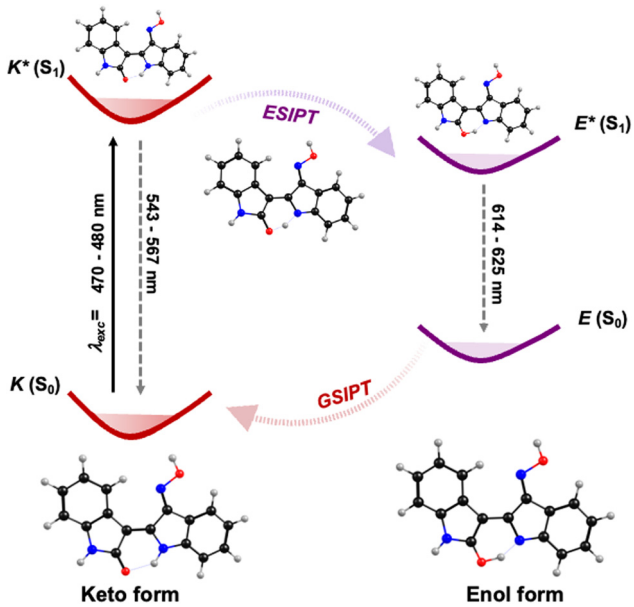

Scheme 2 Schematic diagram of the ESPT process in oxime–indirubin derivatives (in dioxane) based on single-molecule tautomerization, here illustrated for INROx.

Therefore, the E* form of oxime–indirubin derivatives, INROx–OH, can now be generated. The bond distance values show that in both S_0 and S_1, the N–H···O=C hydrogen bond distance is reduced in INROx, suggesting a more favourable intramolecular excited-state proton transfer (ESPIT) than that observed with INR. The small hydrogen bond length value obtained in the keto form (K-S_1) indicates that the central nitrogen has a stronger affinity for the proton in the excited state, facilitating an ultrafast ESIPT.

Considering all the above, and taking into account the spectral and structural characteristics of these conformers, the following aspects should be highlighted: (i) for all the oxime–indirubin derivatives, conformer C (Fig. SI18, ESI†) is found to be the most stable; (ii) the calculated absorption maxima is predicted to be in different solvents, to be in the range of 470–478 nm, which agrees reasonably well with the experimental λ_{max}; (iii) TDDFT calculations predict an emission band at 543–567 nm for the keto form and an emission band around 614–625 nm for the enol form, in good agreement with the experimental values obtained for the oxime–indirubin derivatives in different solvents (see Tables SI3–SI5, ESI†).

The global picture of the decay mechanism, both in non-polar and polar solvents, for INROx, MINROx and 6-BrINROx, can be detailed by combining steady-state and time-resolved data with TDDFT calculations. Upon photoexcitation, electronic charge redistribution results in a higher acidity for the hydrogen bond donor group and an increased basicity for the hydrogen bond acceptor in the keto (K) form. The keto is the thermodynamically stable form with a tautomerization barrier associated with the formation of an imine-enol tautomer transition state (shown in the dashed frame of Scheme 2). As a result, an extremely fast keto-to-enol phototautomerization event occurs, taking less than 1 ps, with the excited-state keto form (K*) rapidly converting to its excited enol form (E*), which is predicted to have a higher contribution in S_1. After decaying back to its electronic ground state, a reverse proton transfer takes place to produce the original K form – ground state intramolecular proton transfer (GSIPT), see Scheme 2. This process is observed with all the studied oxime–indirubin derivatives. However, in glycerol, which has a high viscosity value, formation of the enol is slowed down, as reflected in the longer decay time values associated with this species, in this solvent (Table 2). The relative energy levels of the enol and keto forms of the compounds can be schematically illustrated in Scheme 2, here exemplified for INROx. The DFT optimized geometries of the ground (S_0) and first singlet excited (S_1) states of both the keto (K) and enol (E) forms of INROx, are depicted in Scheme 2. The efficient ESIPT process, along with an increased Stokes shift, leads to a blue-shift in the emission while maintaining high radiative decay rates values (Table 2).

Conclusions

In this work, we have elucidated the excited state deactivation mechanisms in oxime–indirubin derivatives, which was made

by comparison with indirubin. The oxime group has introduced several distinctive features in these compounds. Like indirubin, oxime–indirubin derivatives undergo ESPT. However, a noteworthy distinction is that ESPT occurs extremely rapidly (in less than 1 ps) with all oxime–indirubin derivatives and in all solvents, with the exception of glycerol. The excited state deactivation process involves ESPT in S_1, followed by a subsequent tautomerization of the formed excited enol, converting it back to its initial keto form. Importantly, this occurs without the formation of the *syn*-rotamer, as previously observed with indirubin. Understanding the fast excited state deactivation processes in oxime–indirubin derivatives provides valuable insights into their photophysical behavior that may be correlated with their biological activity, thereby contributing to the development of potential cytotoxic agents for therapeutic applications.

Experimental

Material and methods

Chemicals were obtained from commercial sources and used as received. All the solvents (spectroscopic or equivalent grade) were used without further purification. Microwave-assisted synthesis was performed using a CEM Discover S-Class single-mode microwave reactor, featuring continuous temperature, pressure and microwave power monitoring. ^{1}H NMR and ^{13}C NMR spectra were recorded on a Bruker Avance III spectrometer with operating frequencies of 400.13 and 101 MHz, respectively. High-resolution mass spectrometry (HRMS) was performed on a Bruker microTOF-Focus mass spectrometer equipped with an electrospray ionization time-of-flight (ESI-TOF) source.

Synthesis

Indirubin-3′-oxime (INROx), (3′*E*)-indirubin-3′-oxime. Indirubin (INR) (100 mg) was used and the obtained red-orange solid was washed with methanol and dichloromethane (90 mg, 85%).

^{1}H NMR (400 MHz, DMSO-d$_6$) δ (ppm): 13.46 (s, 1H, NOH), 11.72 (s, 1H, N′H), 10.69 (s, 1H, NH), 8.63 (d, J = 7.8 Hz, 1H, H4), 8.22 (d, J = 7.6 Hz, 1H, H4′), 7.43–7.38 (m, 2H, H6′-H7′), 7.13 (dd, J = 7.6, 1.28 Hz, 1H, H6), 7.04–7.00 (m, 1H, H5′), 6.95 (dd, J = 7.7, 1.3 Hz, 1H, H5), 6.89 (d, J = 7.8 Hz, 1H, H7). ^{13}C NMR (101 MHz, DMSO-d$_6$) δ (ppm): 170.9 (C2), 151.3 (C3′), 145.2 (C2′), 144.8 (C7′a), 138.3 (C7a), 132.0 (C6′), 127.9 (C4′), 125.9 (C6), 122.9 (C4), 122.6 (C3a), 121.4 (C5′), 120.3 (C5), 116.5 (C3′a), 111.5 (C7′), 108.8 (C7), 98.9 (C3). ESI-MS (m/z): calculated for $C_{16}H_{11}N_3O_2$: 277.28; found $[L + H]^+$: 278.0919.

N-Methylindirubin-3′-oxime (MINROx), (2′*Z*,3′*E*)-1-methyl indirubin-3′-oxime. *N*-Methylindirubin (MINR) (100 mg) was used as reagent for obtaining the corresponding red oxime. The solid obtained was washed with dichlorometane (80 mg, 76%).

^{1}H NMR (400 MHz, DMSO-d$_6$) δ (ppm): 13.52 (s, 1H, NOH), 11.73 (s, 1H, N′H), 8.68 (d, J = 7.4 Hz, 1H, H4), 8.23 (d, J = 7.5 Hz, 1H, H4′), 7.41–7.40 (m, 2H, H6′-H7′), 7.21 (t, J = 7.9 Hz, 1H, H6), 7.05–7.00 (m, 3H, H5′-H5-H7), 3.30 (s, 1H, N-CH$_3$). ^{13}C NMR (101 MHz, DMSO-d$_6$) δ (ppm): δ = 169.0 (C2), 151.2 (C3′), 145.4 (C2′), 144.8 (C7′a), 139.5 (C7a), 132.0 (C6′), 127.9 (C4′), 125.9 (C6), 122.7 (C4), 121.8 (C3a), 121.6 (C5′), 120.9 (C5), 116.5 (C3′a), 111.6 (C7′), 107.6 (C7), 98.0 (C3), 25.7 (N-CH$_3$). ESI-MS (m/z): calculated for $C_{17}H_{13}N_3O_2$: 291.31; found $[L + H]^+$: 292.1075.

6-Bromoindirubin-3′-oxime (6-BrINROx), (2′*Z*,3′*E*)-6-bromoindirubin-3′-oxime. 6-Bromoindirubin (6-BrINR) (100 mg) was used as a starting material and the removal of the solvent after the completion of the reaction gave a reddish solid that was washed with methanol and cold dichloromethane (80 mg, 77%).

^{1}H NMR (400 MHz, DMSO-d$_6$) δ (ppm): 13.61 (s, 1H, NOH), 11.75 (s, 1H, N′H), 10.83 (s, 1H, NH), 8.55 (d, J = 8.5 Hz, 1H, H4), 8.22 (d, J = 7.5 Hz, 1H, H4′), 7.43–7.39 (m, 2H, H6′-H7′) 7.11–7.04 (m, 3H, H5′-H5-H7). ^{13}C NMR (101 MHz, DMSO-d$_6$) δ (ppm): 170.6 (C2), 151.3 (C3′), 145.9 (C2′), 144.7 (C7′a), 139.6 (C7a), 132.1 (C6′), 127.9 (C4′), 124.2 (C4), 122.7 (C3a), 122.8 (C5′), 122.0 (C5), 117.8 (C6), 116.4 (C3′a), 111.7 (C7′), 111.5 (C7), 97.7 (C3). ESI-MS (m/z): calculated for $C_{16}H_{10}BrN_3O_2$: 355.00; found $[L + H]^+$: 356.0025.

Photophysical measurements

Absorption spectra were recorded on a Shimadzu UV-2600. Fluorescence spectra were recorded in a Horiba-Jobin-Yvon Spex Fluorolog 3-2.2. spectrophotometer and corrected for the instrumental response of the system. The fluorescence quantum yields of the compounds were determined using indirubin (ϕ_F = 0.0003 in DMF).[21]

Femtosecond Transient Absorption Spectroscopy (fs-TA) experiments were performed with a Helios spectrometer (Ultrafast Systems) with an instrumental response function of ~250 fs. The instrumental response function of the system was assumed to be equal to that of the pump–probe cross correlation determined from the measurement of the instantaneous stimulated Raman signal from the pure solvent (in a 2 mm cuvette). To avoid photodegradation, the solutions were stirred during the experiments or in movement using a motorized translating sample holder. The spectral chirp of the data was corrected using the Surface Xplorer PRO program from Ultrafast Systems.

Fluorescence decays were measured using a broad band femtosecond fluorescence Up-Conversion, fs-UC, Halcyone Fire spectrometer from Ultrafast Systems (thermoelectrically cooled, −40 °C, CCD detectors with spectral range from the UV, ~270–400 nm, Vis, 400–800 nm, to the NIR, ~800–1600 nm), pumped by a 1 kHz Spectra Physics Solstice-Ace laser (7 W, 800 nm and 120 fs IRF) coupled to an TOPAS Prime optical parametric amplifier (OPA) with 235–2600 nm automatic tuning range. The fs-UC spectrometer comprises a delay stage and Ultrafast Systems OPA to generate the gate pulse at 800 nm or 1300 nm with a time resolution of 100 femtoseconds and time window for acquisition up to 8 nanoseconds. The time-resolved fluorescence spectra were obtained with excitation at 450 nm and 530 nm by sum frequency of the fluorescence emission with an 800 nm gate pulse in a BBO crystal. Global analysis of

the data was performed using principal component Analysis *via* single value decomposition (SVD) implemented in the Surface Xplorer Pro program package from Ultrafast Systems.

Quantum electronic calculations

All theoretical calculations were of the DFT type, carried out using GAMESS-US[37] version R3, using as functional the implemented version of LC-BPBE (ω = 0.20 au^{-1}). In TDDFT calculations of FC (Franck–Condon) excitations the dielectric constant of the solvent was split into a ''bulk'' component and a fast component, which is essentially the square of the refractive index. In ''adiabatic'' conditions only the static dielectric constant is used. A 6-31G** basis set was used in either DFT or TDDFT calculations.

The results obtained with the LC-BPBE(20) functional are essentially unscaled raw data from calculations; for the $S_0 \rightarrow S_n$ transitions, a small correction, which result in the subtraction of 0.05 eV, to account for the difference between zero point and the first vibronic level, was considered. For the resulting optimized geometries time dependent DFT calculations (using the same functional and basis set as those in the previously calculations) were performed to predict the vertical electronic excitation energies. Molecular orbital contours were plotted using ChemCraft 1.7 program. Frequency analysis for each compound were also computed and did not yield any imaginary frequencies, indicating that the structure of each molecule corresponds to at least a local minimum on the potential energy surface.

Author contributions

Danîela C. Nobre: investigation, writing – review & editing. Estefanía Delgado-Pinar: methodology, writing – review & editing. Carla Cunha: formal analysis, writing – review & editing. J. Sérgio Seixas de Melo: funding acquisition, conceptualization, project administration, supervision, writing – original & final draft.

Conflicts of interest

The authors declare that there are no conflicts to declare.

Acknowledgements

We acknowledge funding by FEDER (Fundo Europeu de Desenvolvimento Regional) through COMPETE (Programa Operacional Factores de Competitividade). The Coimbra Chemistry Centre – Institute of Molecular Sciences (CQC-IMS) is supported by the Fundação para a Ciência e a Tecnologia (FCT), Portuguese Agency for Scientific Research, through Projects UIDB/00313/2020 and UIDP/00313/2020. E. D.-P. thanks M. Zambrano contract UP2021-044 from the Spanish MICINN financed by the European Union, Next Generation EU. FCT is also acknowledged for PhD Grants: D. C. N. (ref. SFRH/BD/140890/2018) and C. C. (ref. 2020.09661.BD). NMR data collected at the UC-NMR facility are supported in part by the EDRF through the COMPETE Program and by national funds from the FCT through grants RECI/QEQ-QFI/0168/2012 and CENTRO-07-CT62-FEDER-002012, and also through support to Rede Nacional de Ressonância Magnética Nuclear (RNRMN) and to Coimbra Chemistry Centre through grant UID/QUI/00313/2019. Dr João Pina is acknowledged for the technical help in the fs-TA and fs-UC measurements.

References

1 D. Olivier, M.-A. Poincelot, S. Douillard, C. Lefevre, J. Moureau, Y. Ferandin, K. Bettayeb, Z. Xiao, P. Magiatis and L. Skaltsounis, *Photochem. Photobiol. Sci.*, 2008, **7**, 328–336.
2 T. Blažević, E. H. Heiss, A. G. Atanasov, J. M. Breuss, V. M. Dirsch and P. Uhrin, *J. Evidence-Based Complementary Altern. Med.*, 2015, **2015**, 654098.
3 N. Gaboriaud-Kolar, K. Vougogiannopoulou and A.-L. Skaltsounis, *Expert Opin. Ther. Pat.*, 2015, **25**, 583–593.
4 E. A. Perpète and D. Jacquemin, *THEOCHEM*, 2009, **914**, 100–105.
5 L. Meijer, J. Shearer, K. Bettayeb and Y. Ferandin, *Int. Congr. Ser.*, 2007, **1304**, 60–74.
6 G. M. Cragg and D. J. Newman, *J. Nat. Prod.*, 2012, **75**(3), 311–335.
7 F.-F. Yang, M.-S. Shuai, X. Guan, M. Zhang, Q.-Q. Zhang, X.-Z. Fu, Z.-Q. Li, D.-P. Wang, M. Zhou and Y.-Y. Yang, *RSC Adv.*, 2022, **12**, 25068–25080.
8 W. Wang, Y. Wu, H. Xu, Y. Shang, Y. Chen, M. Yan, Z. Li and D. R. Walt, *Ind. Crops Prod.*, 2019, **141**, 111783.
9 D. T. Nguyen, G. N. Truong, T. Van Vuong, T. N. Van, C. N. Manh, C. T. Dao, T. D. T. Thuy, C. L. Van and V. T. Khac, *Chem. Pap.*, 2019, **73**, 1083–1092.
10 R. Jautelat, T. Brumby, M. Schäfer, H. Briem, G. Eisenbrand, S. Schwahn, M. Krüger, U. Lücking, O. Prien and G. Siemeister, *ChemBioChem*, 2005, **6**, 531–540.
11 S. Hu, W. Cui, Z. Zhang, S. Mak, D. Xu, G. Li, Y. Hu, Y. Wang, M. Lee and K. W. Tsim, *J. Mol. Neurosci.*, 2015, **57**, 561–570.
12 L. Meijer, A. L. Skaltsounis, P. Magiatis, P. Polychronopoulos, M. Knockaert, M. Leost, X. Z. P. Ryan, C. A. Vonica, A. Brivanlou, R. Dajani, C. Crovace, C. Tarricone, A. Musacchio, S. M. Roe, L. Pearl and P. Greengard, *Chem. Biol.*, 2003, **10**, 1255–1266.
13 G. Eisenbrand, F. Hippe, S. Jakobs and S. Muehlbeyer, *J. Cancer Res. Clin. Oncol.*, 2004, **130**, 627–635.
14 J. Ribas, K. Bettayeb, Y. Ferandin, M. Knockaert, X. Garrofe-Ochoa, F. Totzke, C. Schächtele, J. Mester, P. Polychronopoulos and P. Magiatis, *Oncogene*, 2006, **25**, 6304–6318.
15 O. Choi, Y. Cho, S. Choi, S. Lee, S. Seo, H. Kim, G. Han, D. Min, T. Park and K. Choi, *Int. J. Obes.*, 2014, **38**, 1044–1052.
16 I. A. Schepetkin, M. B. Plotnikov, A. I. Khlebnikov, T. M. Plotnikova and M. T. Quinn, *Biomolecules*, 2021, **11**, 777.

17 S.-J. Choi, J.-E. Lee, S.-Y. Jeong, I. Im, S.-D. Lee, E.-J. Lee, S. K. Lee, S.-M. Kwon, S.-G. Ahn and J.-H. Yoon, *J. Med. Chem.*, 2010, **53**, 3696–3706.
18 Y. Ichimaru, H. Saito, T. Uchiyama, K. Metori, K. Tabata, T. Suzuki and S. Miyairi, *Bioorg. Med. Chem. Lett.*, 2015, **25**, 1403–1406.
19 S. M. M. Lopes, M. Pineiro and E. M. T. Pinho, *Molecules*, 2020, **25**, 3450.
20 P. Polychronopoulos, P. Magiatis, A.-L. Skaltsounis, V. Myrianthopoulos, E. Mikros, A. Tarricone, A. Musacchio, S. M. Roe, L. Pearl, M. Leost, P. Greengard and L. Meijer, *J. Med. Chem.*, 2004, **47**, 935–946.
21 D. C. Nobre, E. Delgado-Pinar, C. Cunha, A. M. Galvão and J. S. Seixas de Melo, *Dyes Pigm.*, 2023, **212**, 111116.
22 G.-J. Zhao and K.-L. Han, *Acc. Chem. Res.*, 2012, **45**, 404–413.
23 J. S. Seixas de Melo, in *Photochemistry*, ed S. Crespi and S. Protti, The Royal Society of Chemistry, 2022, vol. 49, pp. 31–52.
24 D. Pinheiro, M. Pineiro, A. M. Galvão and J. S. Seixas de Melo, *Chem. Sci.*, 2021, **12**, 303–313.
25 J. Pina, D. Sarmento, M. Accoto, P. L. Gentili, L. Vaccaro, A. Galvão and J. S. Seixas de Melo, *J. Phys. Chem. B*, 2017, **121**, 2308–2318.
26 J. S. Seixas de Melo and A. L. Maçanita, *J. Phys. Chem. B*, 2015, **119**, 2604–2610.
27 J. S. Seixas de Melo, J. Pina, F. B. Dias and A. L. Maçanita, in *Applied Photochemistry*, ed. R. C. Evans, P. Douglas and H. D. Burrow, Springer, Netherlands, Dordrecht, 2013, pp. 533–585.
28 J. Waluk, in *Conformational Analysis of Molecules in Excited States*, ed J. Waluk, Wiley-VCH, New York, 1st edn, 2000.
29 C. A. Rumble, J. Breffke and M. Maroncelli, *J. Phys. Chem. B*, 2017, **121**, 630–637.
30 T. Kumpulainen, B. Lang, A. Rosspeintner and E. Vauthey, *Chem. Rev.*, 2017, **117**, 10826–10939.
31 C. Sun, X. Su, Q. Zhou and Y. Shi, *Org. Chem. Front.*, 2019, **6**, 3093–3100.
32 P. P. Roy, J. Shee, E. A. Arsenault, Y. Yoneda, K. Feuling, M. Head-Gordon and G. R. Fleming, *J. Phys. Chem. Lett.*, 2020, **11**, 4156–4162.
33 Y. Shiraishi, C. Yamada and T. Hirai, *RSC Adv.*, 2019, **9**, 28636–28641.
34 J. S. Seixas de Melo, C. Cabral, J. C. Lima and A. L. Maçanita, *J. Phys. Chem. A*, 2011, **115**, 8392–8398.
35 J. Seixas de Melo and A. L. Macanita, *Chem. Phys. Lett.*, 1993, **204**, 556–562.
36 W. R. Laws and L. Brand, *J. Phys. Chem.*, 1979, **83**, 795–802.
37 M. W. Schmidt, K. K. Baldridge, J. A. Boatz, S. T. Elbert, M. S. Gordon, J. H. Jensen, S. Koseki, N. Marsunaga, K. A. Nguyen, S. Su, T. L. Windus, M. Dupuis and J. A. Mongomery Jr., *J. Comput. Chem.*, 1993, **14**, 1347–1363.